



Cite this: *J. Mater. Chem. B*, 2019,  
7, 2338

## A non-enzymatic glucose sensor based on a CoNi<sub>2</sub>Se<sub>4</sub>/rGO nanocomposite with ultrahigh sensitivity at low working potential†

Bahareh Golrokh Amin,  Jahangir Masud  and Manashi Nath \*

Uniform and porous CoNi<sub>2</sub>Se<sub>4</sub> was successfully synthesized by electrodeposition onto a composite electrode comprising reduced graphene oxide (rGO) anchored on a Ni foam substrate (prepared hydrothermally). This CoNi<sub>2</sub>Se<sub>4</sub>-rGO@NF composite electrode has been employed as an electrocatalyst for the direct oxidation of glucose, thereby acting as a high-performance non-enzymatic glucose sensor. Direct electrochemical measurement with the as-prepared electrode in 0.1 M NaOH revealed that the CoNi<sub>2</sub>Se<sub>4</sub>-rGO nanocomposite has excellent electrocatalytic activity towards glucose oxidation in an alkaline medium with a sensitivity of 18.89 mA mM<sup>-1</sup> cm<sup>-2</sup> and a wide linear response from 1 μM to 4.0 mM at a low applied potential of +0.35 V vs. Ag|AgCl. This study also highlights the effect of decreasing the anion electronegativity on enhancing the electrocatalytic efficiency by lowering the potential needed for glucose oxidation. The catalyst composite also exhibits high selectivity towards glucose oxidation in the presence of several interferences normally found in physiological blood samples. A low glucose detection limit of 0.65 μM and long-term stability along with a short response time of approximately 4 seconds highlights the promising performance of the CoNi<sub>2</sub>Se<sub>4</sub>-rGO@NF electrode for non-enzymatic glucose sensing with high precision and reliability.

Received 17th January 2019,  
Accepted 22nd February 2019

DOI: 10.1039/c9tb00104b

rsc.li/materials-b

### 1. Introduction

Diabetes is a sophisticated and increasingly prevalent condition that affects millions of people worldwide and has become the third main cause of death. Constant monitoring of the glucose level is the most effective way of controlling diabetes and preventing life-threatening conditions.<sup>1</sup> Among various methods available for detection of glucose level, electrochemical detection techniques based on direct glucose electro-oxidation have received significant recognition over the past few years due to their high sensitivity, low limit of detection, promising response time, and low cost.<sup>2,3</sup> Out of the two main categories of electrochemical sensors, the traditional enzymatic glucose sensors suffer from several disadvantages, including the complicated immobilization process of the enzymes, sensitivity to the environmental conditions, poor long-term functional stability of the sensor device, and high fabrication cost.<sup>4–6</sup> To overcome the intrinsic limitations of enzyme-based devices, researchers have intensified investigations into developing

non-enzymatic electrochemical glucose sensing, which relies heavily on direct glucose oxidation on the electrode surface.<sup>7,8</sup> The choice of glucose oxidation electrocatalyst plays a crucial role in the development of such non-enzymatic glucose sensors. Several redox-active compounds have been used as electrocatalysts for glucose electro-oxidation.<sup>9–14</sup> Recently, transition-metal-based compounds have been extensively explored as suitable glucose sensing candidates due to their high electrocatalytic activity, electrical conductivity, abundance, and low cost.<sup>15,16</sup>

Transition metal chalcogenides (TMCs), in particular, have been the subject of intense research in various energy-related applications, such as bifunctional electrocatalysts for water splitting,<sup>17–20</sup> dye-sensitized solar cells,<sup>21–23</sup> Li-ion batteries,<sup>24,25</sup> and supercapacitors.<sup>26–30</sup> The tunable redox-active reaction centers of TMCs improve their electrochemical behavior, while their narrow bandgap and higher degree of covalency lead to better electrical conductivity.<sup>31</sup> Such properties make transition metal chalcogenides significantly better electrocatalysts compared to their respective oxide counterparts, owing to their superior charge transport properties and redox tunability, essential for an electrochemical reaction.<sup>32</sup> Among several types of TMC, Ni-based nanomaterials have been extensively investigated due to their desirable electrocatalytic activity in alkaline electrolytes arising from the tunability of the Ni<sup>2+</sup>/Ni<sup>3+</sup> redox couple, low toxicity, and low cost.<sup>33–35</sup> In addition to binary

Department of Chemistry, Missouri University of Science & Technology, Rolla, MO 65409, USA. E-mail: nathm@mst.edu

† Electronic supplementary information (ESI) available: Characterization techniques such as EDS, SEM and elemental mapping, TEM, and XPS. CV of rGO on Ni foam in the presence of glucose. See DOI: 10.1039/c9tb00104b

selenides, ternary mixed metal selenides have also been explored, primarily to study the effect of transition metal doping on the catalytic activity. Among the ternary selenides, spinel-type compositions having the general formula  $AB_2Se_4$  have been investigated recently for electrocatalytic activity in water splitting.<sup>17,36</sup> In these spinels, the Ni atom is frequently stabilized in the 3+ oxidation state, which is more catalytically active than  $Ni^{2+}$ , thereby increasing their inherent catalytic activity.<sup>17,37</sup> Similarly, in  $CoNi_2Se_4$ , while Co and Ni both exhibit octahedral coordination, the Ni cation occupies the vacancy ordered sites, while the Co cations are present in the fully filled layer, providing several catalytically active sites and numerous pathways for possible charge transport, as well as exposure to the electrolyte.<sup>38</sup>

Apart from the catalyst composition, the other aspect of enhancing electrocatalytic efficiency is increasing the conductivity of the catalytic composite. In this regard, various carbon-based additives have been used. Graphene, being a two-dimensional single-atom thick sheet of carbon atoms arranged in a hexagonal network with a large specific area and exhibiting excellent thermal and electrical conductivity, has been used as a matrix to boost the electron transfer rates and electrocatalytic activities.<sup>39–44</sup>

Inspired by the advantages of  $CoNi_2Se_4$  and graphene-based composites as electrocatalysts, in this study, a  $CoNi_2Se_4$ -rGO composite (rGO = reduced graphene oxide) was pursued as an electrocatalyst for glucose oxidation.  $CoNi_2Se_4$  was successfully synthesized *via* single-step electrodeposition directly onto a composite electrode comprising hydrothermally prepared reduced graphene oxide anchored on a Ni foam substrate ( $CoNi_2Se_4$ -rGO@NF), and was examined for non-enzymatic glucose oxidation for the first time. The developed catalytic composite exhibits an exceptionally high efficiency for glucose oxidation, including an extremely low working potential of only 0.35 V *vs.*  $Ag|AgCl$  with a superior sensitivity of  $18890 \mu A mM^{-1} cm^{-2}$ , a wide linear range of 1  $\mu M$  to 4.0 mM for glucose detection, a low detection limit of 0.65  $\mu M$  ( $S/N = 3$ ), excellent stability, and high selectivity in the presence of interfering species. The electrochemical sensing behavior of the  $CoNi_2Se_4$ -rGO@NF electrode towards glucose sensing was investigated using amperometric techniques and is presented in the following sections.

## 2. Experimental

### 2.1 Materials

All reagents were of analytical grade and used as purchased without further purification. Nickel acetate tetrahydrate [ $Ni(C_2H_4O_2)_2 \cdot 4H_2O$ ] was purchased from J. T. Baker chemical company, USA, and cobalt acetate tetrahydrate [ $Co(C_2H_4O_2)_2 \cdot 4H_2O$ ] was acquired from Alfa Aesar.  $SeO_2$  [Acros Chemicals], lithium chloride (LiCl) [Aldrich], dextrose [Sigma-Aldrich], ascorbic acid [Fisher-Scientific], lactose [Fisher-Scientific], fructose [Aldrich], dopamine [Sigma-Aldrich], sodium chloride and potassium chloride [Fisher-Scientific] were all acquired and used throughout the experiment. Ni foam was employed as the substrate in the electrodeposition process. Deionized water ( $18.2 M\Omega cm^{-1}$ ) was used throughout the work.

### 2.2 Synthesis of graphene oxide (GO) and rGO samples

Graphene oxide (GO) was first prepared by a modified Hummers' method using natural graphite, following a reported procedure.<sup>45</sup> Specifically, 10 mg of GO was dispersed in 12 mL of DI water and sonicated for 45 minutes. Then, 3  $\mu L$  of hydrazine monohydride was added to this dispersion and was sonicated for another 30 minutes. Ni foam was cleaned using diluted HCl followed by sonication in a mixture of ethanol and deionized water. Both the GO mixture and the pre-cleaned Ni foam were transferred into a 23 mL Teflon-lined stainless steel autoclave, which was sealed and kept at 145 °C for 8 hours and then naturally cooled to room temperature. The Ni foam with the rGO ingrown on the surface was taken out and rinsed with DI water and ethanol several times, followed by drying in a vacuum oven at 40 °C overnight.

### 2.3 Synthesis of $CoNi_2Se_4$ @NF and $CoNi_2Se_4$ -rGO@NF

As described in our previous work,<sup>17</sup>  $CoNi_2Se_4$  can be synthesized by electrodeposition. A similar synthesis strategy was followed in this paper where electrodeposition was carried out from an electrolyte containing 10 mM  $Ni(C_2H_4O_2)_2 \cdot 4H_2O$ , 25 mM  $Co(C_2H_4O_2)_2 \cdot 4H_2O$ , and 40 mM  $SeO_2$  dissolved in DI water. Dilute HCl was added to the solution to adjust the pH of the electrolytic bath to 2.5. The mixture was stirred and sonicated for 15 minutes to completely disperse and dissolve the precursors, and then nitrogen gas was purged through the solution for 35 minutes.  $CoNi_2Se_4$  was electrodeposited from the electrolytic bath at a potential of  $-0.8$  V (*vs.*  $Ag|AgCl$ ) for 600 seconds at room temperature. Electrodeposition was performed on both rGO-coated Ni foam and bare Ni foam for comparison of the electrocatalytic activities and to investigate the influence of rGO. Fig. 1 shows a detailed schematic of the growth process of the  $CoNi_2Se_4$ -rGO@NF catalytic composite. After each electrodeposition, the as-grown thin films were washed with deionized water to remove impurities and unreacted ions from the surface. For electrochemical measurements, the prepared electrode was covered with Teflon tape, leaving an exposed geometric area of  $0.283 cm^2$ .

### 2.4 Characterization of the materials

The crystalline phase of the product was characterized through powder X-ray diffraction (PXRD) on a Philips X-Pert X-ray diffractometer with Cu  $K\alpha$  ( $1.5418 \text{ \AA}$ ) radiation. The PXRD pattern was collected from  $10^\circ$  to  $90^\circ$ . A FEI Helios Nanolab 600 FIB/FESEM operating at an acceleration voltage of 10 kV and a working distance of 5.0 mm was employed to obtain SEM images of the electrode surface to study the morphology of the product. Also, energy dispersive spectroscopy (EDS) accompanied by line scan analysis was acquired from the SEM microscope. High resolution transmission electron microscopy (TEM) images

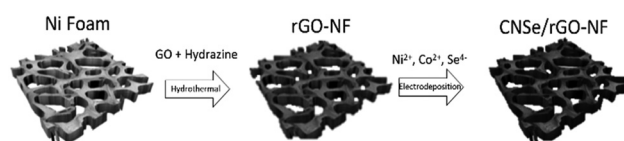


Fig. 1 Schematic of the fabrication process of  $CoNi_2Se_4$ -rGO@NF.

and selected area electron diffraction (SAED) patterns were obtained using an FEI TECNAI F20 operating at 200 kV acceleration voltage. X-ray photoelectron spectroscopy (XPS) measurements of the catalysts were performed by a Kratos Axis 165 X-ray Photoelectron Spectrometer using a monochromatic Al X-ray source. The spectra were collected after sputtering with Ar for 30 seconds, which removes approximately <1 nm from the surface.

## 2.5 Electrochemical measurements

The electrochemically active surface area (ECSA) of the modified electrode from double layer capacitance measurements in the non-Faradaic region was also measured and details are provided in the ESI† (Fig. S1). In the non-Faradaic region, the current measured corresponded only to the charge/discharge of the electric double layer. A series of current-voltage plots were measured in the non-Faradaic region with scan rates ranging from 2.5–40 mV s<sup>-1</sup>. The current at a fixed potential was plotted as a function of scan rate, and from the linear plot, the double layer capacitance,  $C_{dl}$ , was estimated. ECSA was calculated using the following equation (eqn (1)):<sup>17</sup>

$$ECSA = C_{dl}/C_s \quad (1)$$

where  $C_s$  is the specific capacitance of the sample or the capacitance of an atomically smooth planar surface of the material per unit area under identical electrolyte conditions ( $C_s = 0.04 \text{ mF cm}^{-2}$  in 0.1 M NaOH was used). The ECSA was estimated to be 80 cm<sup>2</sup>.

Cyclic voltammetry (CV) and chronoamperometry measurements were performed with an IviumStat potentiostat under continuous stirring in a three-electrode electrochemical setup to scan the current and voltage profiles, where CoNi<sub>2</sub>Se<sub>4</sub>-rGO@NF served as the working electrode while a platinum mesh and Ag|AgCl electrode were selected as the counter and reference electrodes, respectively. A 0.1 M NaOH aqueous solution was used as the electrolyte.

The limit of detection of the analyte was calculated according to the following equation (eqn (2)):<sup>46–48</sup>

$$LOD = 3SD/N \quad (2)$$

where SD is the standard deviation of the analyte concentration calculated from the current response after consecutive addition of glucose into the electrolyte; N is the slope of the calibration curve, which indicates the sensitivity of the electrode with a signal-to-noise ratio of 3.

## 3. Results and discussion

### 3.1 Characterization of the CoNi<sub>2</sub>Se<sub>4</sub>-rGO@NF sample

The catalytic films were grown directly on rGO-coated Ni foam, since Ni foam is a conductive substrate with a 3-dimensional porous network that facilitates electron transport between the electrodeposited nanostructure and the electrolyte, thus making it a desirable platform for the fabrication of biosensors. The morphology of the as-synthesized rGO@NF and electrodeposited CoNi<sub>2</sub>Se<sub>4</sub>-rGO@NF as the final product was observed

by scanning electron microscopy (SEM). Fig. 2a and its inset show low- and high-magnification SEM images, respectively, of pure binder-free rGO grown on Ni foam. Fig. 2b and its inset and Fig. 2c show the CoNi<sub>2</sub>Se<sub>4</sub> films grown on the rGO@Ni substrate with low to high magnifications. As shown in these figures, both rGO and the nanoflake-like structures of CoNi<sub>2</sub>Se<sub>4</sub>-rGO were uniformly distributed on the Ni foam. Such a flake-like nanostructured geometry leads to a rough surface of the electrode, which can be expected to lead to enhancement of the electrode performance due to the high surface area, better surface-to-volume ratio and exposure of more electrocatalytically active sites on CoNi<sub>2</sub>Se<sub>4</sub>-rGO@NF. Moreover, the surface composition of the CoNi<sub>2</sub>Se<sub>4</sub> nanoflakes has been investigated through EDS spectra (Fig. S2, ESI†), which verified the film composition to be CoNi<sub>2</sub>Se<sub>4</sub> with an approximate elemental ratio of 1:2:4 for Co:Ni:Se.

In addition, the elemental mapping of Co, Ni, and Se (Fig. S3, ESI†) further confirmed the coexistence of Co, Ni and Se uniformly over the Ni foam in the above-mentioned relative ratio. The nanostructured morphology of the electrodeposited film was further verified by TEM imaging as has been reported in our previous article on CoNi<sub>2</sub>Se<sub>4</sub> as an efficient OER electrocatalyst (Fig. S4a, ESI†).<sup>17</sup> The SAED pattern shows the crystalline nature of the nanocomposite (Fig. S4b, ESI†). The crystalline phase of the material was also confirmed by the powder X-ray diffraction (PXRD) method, as illustrated in Fig. 2d. The diffraction peaks from the as-synthesized CoNi<sub>2</sub>Se<sub>4</sub>-rGO@NF film matched with the standard diffraction pattern of CoNi<sub>2</sub>Se<sub>4</sub> (PDF file card no. 04-006-5239) confirming the pure crystalline nature of the electrodeposited film. Raman spectroscopy was also performed to characterize the rGO present in the composite. As shown in Fig. 2e, the as-synthesized rGO shows two prominent peaks at 1331 cm<sup>-1</sup> and 1573 cm<sup>-1</sup> corresponding to the structural defects and disorder in the graphene network (D band) and the C–C bond stretching frequency (G band), respectively. Generally, the intensity ratio of the D- and G-bands ( $I_D/I_G$ ) is used to estimate the degree of disorder and the average size of the sp<sup>2</sup> domains. The value of  $I_D/I_G$  was calculated to be 0.94. Furthermore, XPS was employed to obtain detailed information about the chemical composition and oxidation states of the corresponding elements in the as-deposited CoNi<sub>2</sub>Se<sub>4</sub> nanoflakes. For XPS studies, electrodeposited films on Au-glass substrates were used to avoid the huge Ni signal coming from Ni foam substrate. The XPS studies have also been reported in our previous study.<sup>17</sup> The XPS peaks were calibrated with respect to the C1s signal (284.5 eV) as a reference binding energy. Fig. S5, ESI† (adopted from our previous publication<sup>17</sup>) shows all of the XPS peaks for Ni, Co, and Se. The oxidation states of Co and Ni were investigated from the deconvoluted XPS spectra. It was confirmed, using the Gaussian fitting method, that Ni 2p and Co 2p are present in mixed 2+ and 3+ valence states, which conceivably plays a key role in their electrocatalytic activity towards glucose oxidation.<sup>49</sup> As shown in Fig. S5a, ESI†, the peaks located at 777.6 eV and 794.2 eV can be attributed to Co<sup>3+</sup> and those at 780.2 eV and 795.5 eV are assigned to Co<sup>2+</sup> with its shake-up satellite peaks at 785.2 eV



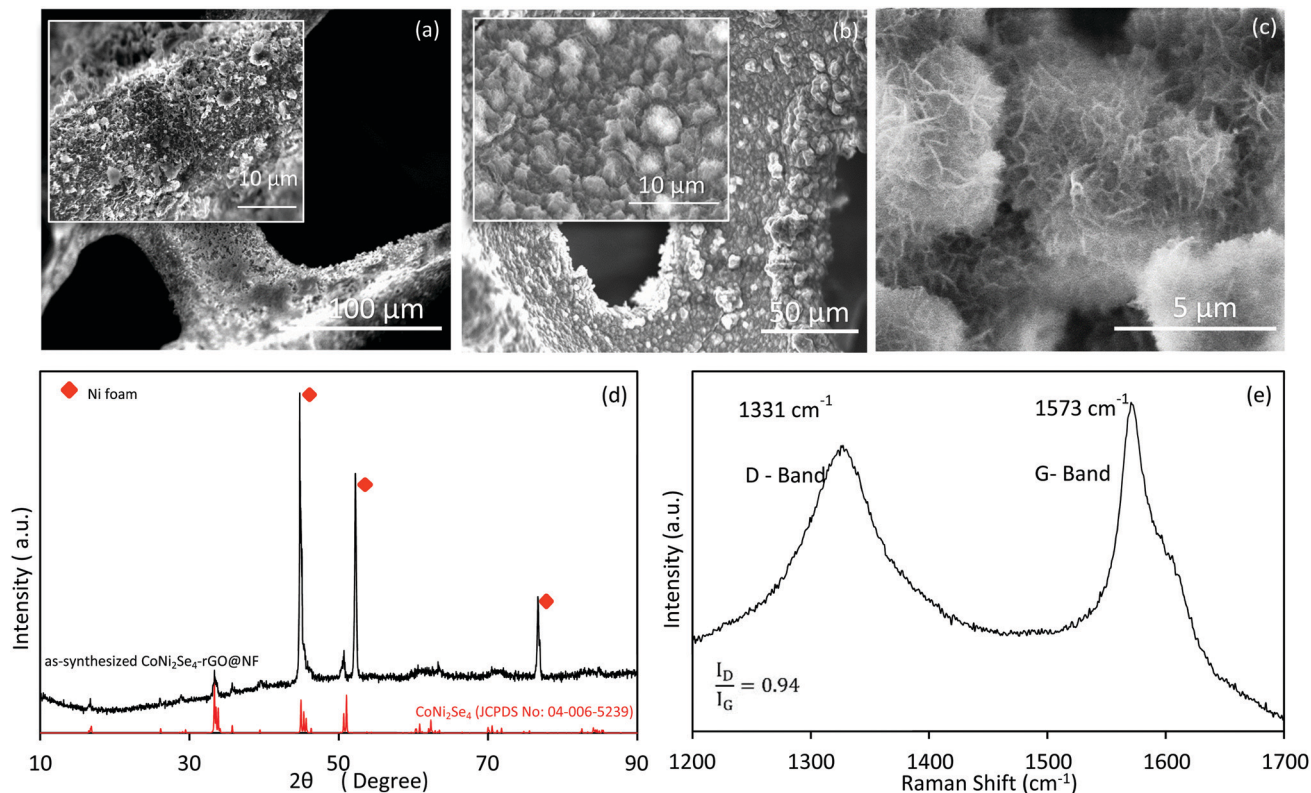


Fig. 2 SEM images of (a) reduced graphene oxide on Ni foam at low magnification (the inset shows a higher magnification SEM image of rGO@NF), (b) CoNi<sub>2</sub>Se<sub>4</sub>-rGO on Ni foam at low magnification (the inset shows a higher magnification SEM image) and (c) CoNi<sub>2</sub>Se<sub>4</sub>-rGO@NF showing a nanoflake geometry with a rough electrode surface. (d) The XRD pattern of CoNi<sub>2</sub>Se<sub>4</sub>-rGO@NF. (e) Raman spectrum of the reduced graphene oxide.

and 800.5 eV.<sup>50,51</sup> The peaks centered at 854.3 eV and 871.8 eV correspond to Ni<sup>2+</sup>, while those at 856.1 and 873.3 eV are in agreement with Ni<sup>3+</sup> (Fig. S5b, ESI†).<sup>52,53</sup> Finally, the peaks at 54.0 eV and 54.9 eV shown in Fig. S5(C) (ESI†) correspond to Se 3d<sub>5/2</sub> and Se 3d<sub>3/2</sub>, respectively, and match with the binding energies repeatedly reported in the transition metal selenides.<sup>54</sup>

Based on the XPS results, it was concluded that CoNi<sub>2</sub>Se<sub>4</sub> has a vacancy-ordered spinel structure, where Co is primarily present as divalent ions occupying the fully-filled layers while Ni is present primarily as Ni<sup>3+</sup> in the half-filled vacancy-ordered layer. The presence of mixed valency also indicates that there is significant scrambling of Co<sup>3+</sup> and Ni<sup>2+</sup> in the vacancy-ordered and fully occupied layers, respectively.

### 3.2 Electrocatalytic activity of the CoNi<sub>2</sub>Se<sub>4</sub>@NF electrode towards glucose detection

Cyclic voltammetry (CV) was used to characterize the electrocatalytic activity of different catalyst-coated composite electrodes towards glucose oxidation in an alkaline medium. Fig. 3a shows the current response of bare CoNi<sub>2</sub>Se<sub>4</sub> on Ni foam measured in 0.1 M NaOH at different scan rates by scanning the applied potential. It is observed that the anodic and cathodic peak currents clearly increase with increasing scan rate, suggesting a diffusion-controlled reaction mechanism at the surface of the electrode. The inset in Fig. 3a shows the linear relationship between the peak current and the square root of the scan rate,

which further verifies the diffusion-controlled process occurring at the electrode. Upon addition of 1.0, 2.0, 3.0, 4.0, and 5.0 mM glucose into the 0.1 M NaOH electrolyte, the CoNi<sub>2</sub>Se<sub>4</sub>@NF electrode exhibited a substantial increase in anodic current density as shown in Fig. 3b, indicating increase of the oxidation current due to glucose oxidation. To clearly identify the optimal potential for glucose oxidation, different applied potentials in the range of 0.3–0.4 V vs. Ag|AgCl were investigated with successive addition of 0.1 mM glucose, as shown in Fig. 3c. It is obvious that the current response on glucose addition increases sharply when the applied potential increases from 0.3 V to 0.35 V and then decreases with the increase of the applied potential from 0.35 to 0.40 V. Therefore, the best working potential for glucose oxidation was selected to be 0.35 V for the remainder of this study. As shown in Fig. 3d, upon successive addition of varying concentrations of glucose, significant and fast current responses were observed for the CoNi<sub>2</sub>Se<sub>4</sub>@NF electrode with 95% of the steady-state current reached within 6 seconds (Fig. 3f). The step size of the current density increase depends on the concentration of glucose and typically rises with increasing concentration (Fig. 3d). The current density was plotted as a function of added glucose concentration as shown in Fig. 3e, which served as the calibration curve for the CoNi<sub>2</sub>Se<sub>4</sub>@NF electrode. Linear fitting of the calibration plot in the concentration range from 0.001 μM to 4.0 mM ( $R^2 = 0.9974$ ) yielded the sensitivity of glucose detection, which was estimated to be as high as 9.8766 mA mM<sup>-1</sup> cm<sup>-2</sup> (Fig. 3e).

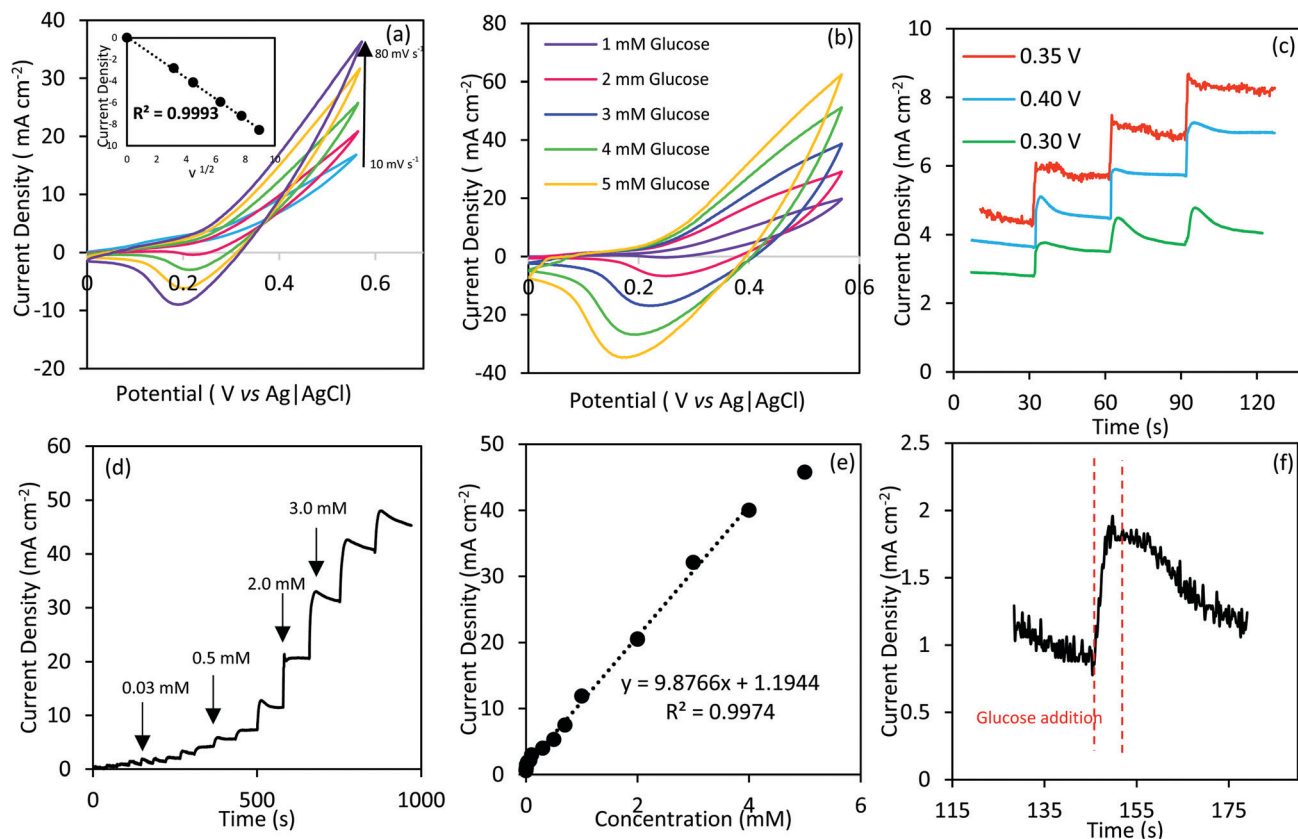


Fig. 3 Cyclic voltammograms of the  $\text{CoNi}_2\text{Se}_4$  on Ni foam electrode: (a) in the absence of glucose at different scan rates: 10, 20, 40, 60, 80, and  $100 \text{ mV s}^{-1}$  (the inset is the relationship between the peak current and the square root of the scan rate), and (b) at different glucose concentrations with a scan rate of  $10 \text{ mV s}^{-1}$ . (c) Amperometric current responses of  $\text{CoNi}_2\text{Se}_4/\text{NF}$  at different working potentials with successive addition of  $0.1 \text{ mM}$  glucose. (d) Amperometric response of  $\text{CoNi}_2\text{Se}_4/\text{NF}$  upon the successive addition of glucose. (e) The calibration curve for the current response to glucose concentration. (f) Plot showing the response time to reach the steady-state current.

In glucose sensing devices, the efficiency is measured by the current response as well as the working potential for the device. Since most of these chalcogenides have limited electrical conductivity, in order to obtain better electrocatalytic performance, rGO was introduced to the  $\text{CoNi}_2\text{Se}_4$  system. It is expected that the presence of rGO in the catalytic matrix will elevate the sensitivity of the electrode with a faster response time and higher current density due to the enhanced conductivity, better electron transfer, and increased specific surface area of the reduced graphene oxide.<sup>55</sup>

### 3.3 Electrocatalytic activity of the $\text{CoNi}_2\text{Se}_4\text{-rGO}/\text{NF}$ electrode towards glucose sensing and detection

The  $\text{CoNi}_2\text{Se}_4\text{-rGO}/\text{NF}$  composite electrode was prepared by a similar electrodeposition technique to that mentioned above. The electrocatalytic performance of the composite  $\text{CoNi}_2\text{Se}_4\text{-rGO}/\text{NF}$  electrode, shown in Fig. 4, was investigated by electrochemical measurements such as chronoamperometry and CV in the absence and presence of glucose in  $0.1 \text{ M NaOH}$  solution at the scan rate of  $10 \text{ mV s}^{-1}$ . The CV plots presented in Fig. 4a show that  $\text{CoNi}_2\text{Se}_4\text{-rGO}/\text{NF}$  does not exhibit a clear anodic peak in the potential range between  $0.1 \text{ V}$  and  $0.5 \text{ V}$ . However, the anodic current rises and shifts linearly with the

increase of the scan rate. The linear relationship between the peak current and the square root of the scan rate as shown in the inset of Fig. 4a indicates a diffusion-controlled electrochemical process occurring on the electrode surface. The cathodic peak shows a negative movement with the increase of the scan rate, most probably due to the fortified electric polarization resulting from the oxidation-reduction procedure.<sup>56</sup>

The electrochemical properties of  $\text{CoNi}_2\text{Se}_4\text{-rGO}/\text{NF}$  towards glucose oxidation are shown in Fig. 4b. Upon injection of glucose into the electrolyte, a clear anodic peak can be observed at  $+0.35 \text{ V vs. Ag}/\text{AgCl}$  in the CV curve, and the enhancement of the oxidation peak becomes more noticeable with an increase in glucose concentration.

By comparing the electrocatalytic activities of the  $\text{CoNi}_2\text{Se}_4/\text{NF}$  and  $\text{CoNi}_2\text{Se}_4\text{-rGO}/\text{NF}$  electrodes, it can be observed that the addition of rGO led to higher oxidation current densities and less noise in the chronoamperometry plots, leading to a more distinctive peak for glucose oxidation. This enhancement can be related to the increased surface area of the rGO- $\text{CoNi}_2\text{Se}_4$  composite, as well as better conductivity of the matrix leading to enhanced electron transfer rate. However, rGO by itself on Ni foam did not show significant electrocatalytic activity towards glucose oxidation as shown in Fig. S6, ESI,† highlighting the

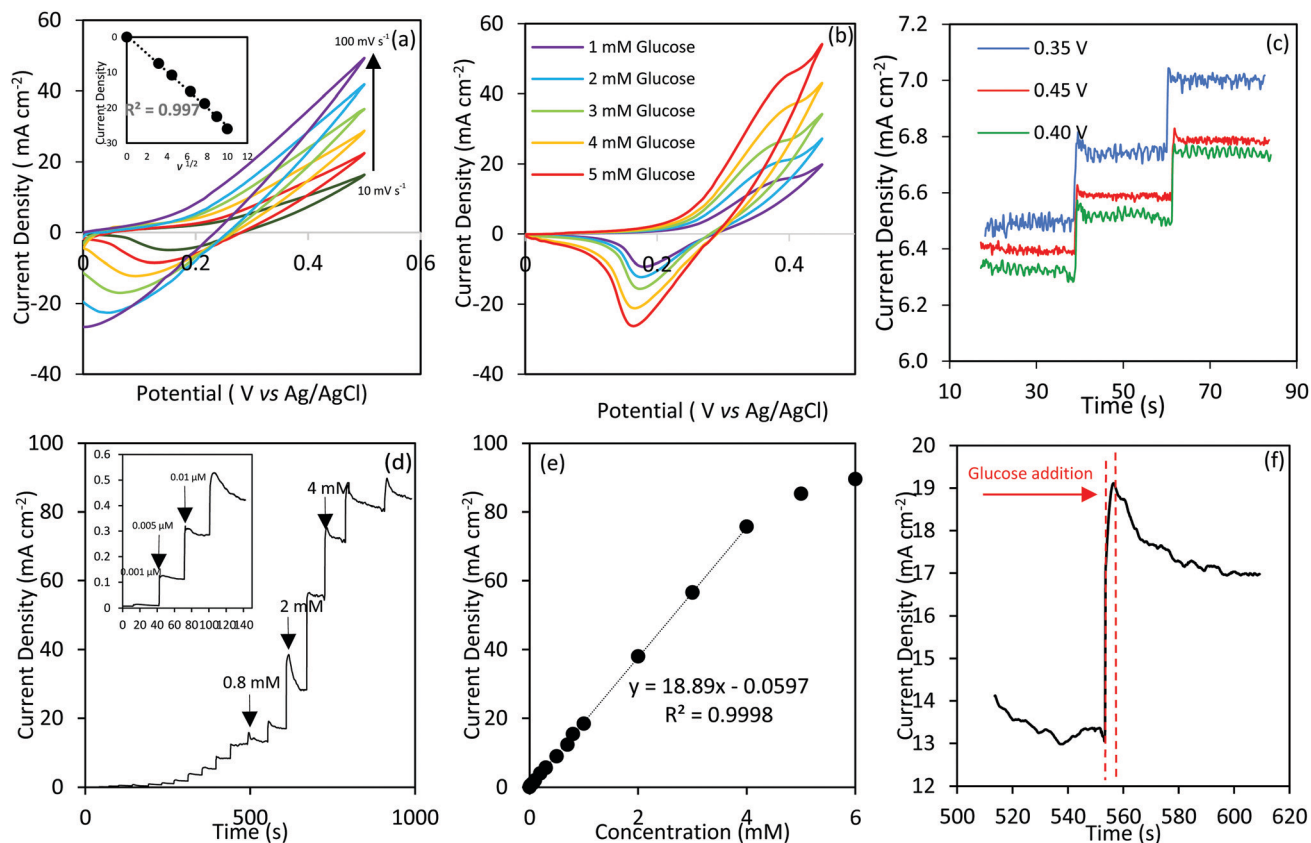


Fig. 4 Cyclic voltammograms of the  $\text{CoNi}_2\text{Se}_4\text{-rGO@NF}$  electrode (a) in the absence of glucose at different scan rates: 10, 20, 40, 60, 80, and  $100 \text{ mV s}^{-1}$ , and (b) at different glucose concentrations with a scan rate of  $10 \text{ mV s}^{-1}$ . (c) Amperometric current responses of  $\text{CoNi}_2\text{Se}_4\text{-rGO@NF}$  at different working potentials with successive addition of  $0.01 \mu\text{M}$  glucose. (d) Amperometric response of  $\text{CoNi}_2\text{Se}_4\text{-rGO@NF}$  upon the successive addition of glucose; (inset) current response upon addition of a low concentration of glucose. (e) The calibration curve for the current response to glucose concentration. (f) Plot of the response time to reach the steady-state current.

fact that the actual catalytically active centers are in the  $\text{CoNi}_2\text{Se}_4$  component (specifically Co and Ni sites).

In order to achieve a high current response for the detection of glucose, choosing an optimized working potential in the presence of glucose is critical. An overly-high potential can lead to an unwanted oxygen evolution reaction resulting in lesser accessible active surface area and large background current. At the same time, detection of glucose in a wide range of concentrations at the optimal applied potential is also critical for practical application of the sensor. In this regard, the amperometric response upon consecutive addition of  $0.01 \mu\text{M}$  glucose to  $0.1 \text{ M NaOH}$  was explored through a typical  $I-t$  technique and illustrated in Fig. 4c. As shown in the figure, the maximum current response was observed at  $0.35 \text{ V vs. Ag|AgCl}$ , which matches well with the anodic oxidation peak, enabling excellent sensing performance for glucose oxidation. Therefore, this potential was selected as the working potential for the rest of the electrochemical experiments.

The amperometric response data of the  $\text{CoNi}_2\text{Se}_4\text{-rGO@NF}$  electrode acquired at  $0.35 \text{ V vs. Ag|AgCl}$  in  $0.1 \text{ M NaOH}$  electrolyte under vigorous stirring of the  $\text{NaOH}$  solution at  $1000 \text{ rpm}$  are provided in Fig. 4d, showing a steep current rise with every successive injection of the glucose analyte with varying concentrations.

As explained above, the sensitivity and linear range of glucose detection can be found by plotting the peak current density against the glucose concentration, as shown in Fig. 4e. In the concentration range between  $1 \mu\text{M}$  and  $4.0 \text{ mM}$ , the sensor response is linear with a sensitivity of  $18.890 \text{ mA mM}^{-1} \text{ cm}^{-2}$  and a correlation coefficient ( $R^2$ ) of  $0.9998$  obtained from linear fitting of the plot shown in Fig. 4e.

To the best of our knowledge, this is one of the highest sensitivities that has been reported at a low operating voltage for non-enzymatic glucose sensors (Table 1). The relatively small linear range of glucose sensing could be due to the limited exposure of the surface active sites of the electrode to the reaction intermediates at high concentrations of glucose. The limit of detection (LOD) for  $\text{CoNi}_2\text{Se}_4\text{-rGO@NF}$  with a signal-to-noise ratio of 3 ( $S/N = 3$ ) for non-enzymatic glucose sensing was found to be as low as  $0.65 \mu\text{M}$  using eqn (2).  $\text{CoNi}_2\text{Se}_4\text{-rGO@NF}$  can reach 95% of its steady-state current signal in less than 4 seconds, as shown in Fig. 4f, which indicates a good electrocatalytic performance of the  $\text{CoNi}_2\text{Se}_4\text{-rGO@NF}$  electrode for non-enzymatic glucose oxidation.

It should be noted here that the sensitivity of this  $\text{CoNi}_2\text{Se}_4\text{-rGO}$  based non-enzymatic sensor is superior to that of the average sensors. The causes of this high sensitivity are manifold: (i) the



Table 1 Comparison of previously reported non-enzymatic glucose sensors with CoNi<sub>2</sub>Se<sub>4</sub>-rGO@NF

Electrode	Detection potential (V)	Sensitivity ( $\mu\text{A mM}^{-1} \text{cm}^{-2}$ )	LOD ( $\mu\text{M}$ )	Linear range	Ref.
CoNi <sub>2</sub> Se <sub>4</sub> -rGO@NF	0.35 vs. Ag AgCl	18 890	0.65	1 $\mu\text{M}$ to 4.0 mM	This work
Solid/nanoporous Au/Co <sub>3</sub> O <sub>4</sub> (in 0.5 M KOH)	0.26 vs. Ag AgCl	12 500	0.005	1 mM to 10 mM	63
CuO nanowires	0.33 vs. Ag AgCl	0.49	0.05	0.4 $\mu\text{M}$ to 2.0 mM	64
NiO-GR/GCE	0.35 vs. Ag AgCl	15.94	5.0	0.02 to 4.5 mM	65
Co <sub>3</sub> O <sub>4</sub> UNS-Ni(OH) <sub>2</sub> /GCE	0.35 vs. Ag AgCl	1.089	1.08	5–40 $\mu\text{M}$	66
Electrodeposited NiCo <sub>2</sub> O <sub>4</sub>	0.40 vs. Ag AgCl	6.69	0.38	5–65 $\mu\text{M}$	67
CuO NWA/CF	0.50 vs. Ag AgCl	32 330	0.02	0.10–0.50 mM	68
NiO/C microspheres	0.50 vs. Ag AgCl	30 190	2.0	2 $\mu\text{M}$ to 1.279 mM	69
Cu <sub>2</sub> Se SPs/CF	0.50 vs. Ag AgCl	18 660	0.25	0.25 $\mu\text{M}$ to 0.237 mM	70
3D Co <sub>3</sub> O <sub>4</sub> /Ni	0.50 vs. Ag AgCl	13 855	1.0	0.04–3.6 mM	71
Ni <sup>3+</sup> -rich surface electrode	0.50 vs. Ag AgCl	11 361; 3579.9	0.9	0.001–1, 2–4 mM	72
3D porous Ni networks	0.50 vs. Ag AgCl	2900	0.07	5 $\mu\text{M}$ to 4 mM	73
NiCo <sub>2</sub> O <sub>4</sub> /3DGF	0.50 vs. Ag AgCl	2524	0.38	Up to 80 mM	74
Ni-Co NSs/rGO	0.50 vs. SCE	1773.61	3.79	10 $\mu\text{M}$ to 2.65 mM	75
Ni <sub>0.31</sub> Co <sub>0.69</sub> S <sub>2</sub> /rGO	0.50 vs. Ag AgCl	1753; 954.7	0.078	1 mM to 5 mM; 5–16 mM	76
CuO NPs	0.50 vs. Ag AgCl	1430	5.0	0.04–6.0 mM	77
NiCoO <sub>2</sub> @CNT	0.50 vs. Ag AgCl	1424	1.14	0.01–1.55 mM	78
NiO/GNS	0.50 vs. Ag AgCl	666.71	5.0	5 $\mu\text{M}$ to 4.2 mM	79
s-NiO/GD	0.50 vs. Ag AgCl	36.13	0.9	Up to 10 mM	80
NiNPs/PEDOT/RGO	0.50 vs. Ag AgCl	36.15	0.8	0.001–5.1 mM	81
NiSe <sub>2</sub> -NS/GCE	0.50 vs. Ag AgCl	5.6	0.023	0.099–1252 $\mu\text{M}$	82
NiCo <sub>2</sub> S <sub>4</sub>	0.50 vs. Ag AgCl	5.14	1.20	1–664 $\mu\text{M}$	83
NiONP/Gr	0.53 vs. Ag AgCl	2401	0.53	0.001–15 mM	84
Co(OH) <sub>2</sub> /GCE	0.53 vs. Ag AgCl	925.21	0.93	Up to 0.13 mM	85
CuNi/C; a metal-organic framework	0.54 vs. Ag AgCl	17 120	0.07	0.2 $\mu\text{M}$ to 2.72 mM	86
Ni <sub>3</sub> S <sub>2</sub> /MWCNT	0.54 vs. Ag AgCl	3345	1.0	30–500 $\mu\text{M}$	87
Ni <sub>3</sub> S <sub>2</sub> /Ni foam	0.55 vs. Ag AgCl	16 460	0.82	0.0005–3 mM	88
3D Ni <sub>3</sub> S <sub>2</sub> /Ni foam	0.55 vs. Ag AgCl	6148	1.2	0.005–3.0 mM	89
CuCo <sub>2</sub> O <sub>4</sub> NWAs/CC	0.55 vs. Ag AgCl	3930	0.50	0.001–0.93 mM	90
NiCo <sub>2</sub> O <sub>4</sub> /rGO	0.55 vs. Ag AgCl	2082.57	0.70	0.04–1.28 mM	91
Co <sub>3</sub> O <sub>4</sub> HND/GCE	0.55 vs. Ag AgCl	708.4	0.58	2.0–6060 $\mu\text{M}$	92
MnCo <sub>2</sub> O <sub>4</sub> nanofibers	0.55 vs. Ag AgCl	679.5	0.01	0.05–800 $\mu\text{M}$	93
Co <sub>3</sub> O <sub>4</sub> /NiCo <sub>2</sub> O <sub>4</sub> DSNCs@G	0.55 vs. Ag AgCl	304	0.384	0.01–3.52 mM	94
Electrospun Co <sub>3</sub> O <sub>4</sub> nanofibers	0.59 vs. Ag AgCl	36.25	0.97	Up to 2.04 mM	95
CuO/rGO/CNT	0.60 vs. Ag AgCl	9278	1.0	0.01–1 mM	96
Ni(OH) <sub>2</sub> nanostructure modified rGO	0.60 vs. Ag AgCl	11 400	15.0	0.01–30 mM	97
CoP NA/TM	0.60 vs. Ag AgCl	5168.6	0.1	0.0005–1.50 mM	98
CuO/NiO/PANI/GCE	0.60 vs. Ag AgCl	3402	2	20 $\mu\text{M}$ –2.5 mM	99
NA/NiONF-rGO/GCE	0.60 vs. Ag AgCl	1100	0.77	0.002–0.60 mM	100
Ni-MWNTs	0.60 vs. Ag AgCl	67.19	0.89	3.2 $\mu\text{M}$ –17.5 mM	101
Nano-SiO <sub>2</sub> -unprotected Pt (enzymatic)	0.60 vs. Ag AgCl	3.85	1.5	0.27–4.08 mM	102
3-D Ni <sub>3</sub> (VO <sub>4</sub> ) <sub>2</sub> nanosheet	0.62 vs. Ag AgCl	19 830	0.57	2.5–150 $\mu\text{M}$	103
CuO-ZnO NRs/FTO	0.62 vs. Ag AgCl	2961.7	0.40	Up to 8.45 mM	104
CuS/RGO/CuS/Cu	0.65 vs. Ag AgCl	22 670	0.50	0.001–0.655 mM	105
Ni/Al-LDH nanosheet film on Ti foil	0.70 vs. Ag AgCl	24.45	5.0	0.005–10.0 mM	106
TiO <sub>2</sub> NTs-Ni(OH) <sub>2</sub> NPs hybrid	0.70 vs. Ag AgCl	120	5.0	0.02–1.70 mM	107

composition of the catalytic site (Co and Ni in a selenide coordination); (ii) the presence of Ni<sup>3+</sup> in the as-prepared catalyst; (iii) the presence of rGO and a highly porous morphology of the electrode; and (iv) the direct growth of the catalytic composite on the electrode yielding a binder-free film. The mechanism of glucose oxidation to gluconolactone is believed to be initiated by the attachment of a hydroxyl group (–OH) to the catalytically active transition metal sites (Ni and Co in this case), which undergo local oxidation. The charge transfer occurring at the catalyst-electrolyte interface can further lead to oxidation of glucose.<sup>57</sup> Since the catalytic site undergoes local oxidation, the redox potential for the transition metal sites can have a large influence on the catalytic activity for glucose oxidation, especially the applied potential value. Recently we have probed the influence of ligand composition on the electrocatalytic activity in transition metal-based catalysts in the context of the OER. From these studies, it has been

observed that increasing the covalency around the transition metal sites by decreasing the ligand electronegativity leads to lowering of the transition metal site oxidation potential. Hence, the selenide coordination of the transition metals lowers the oxidation potential for these catalytically active sites.<sup>58,59</sup> Therefore, the onset of glucose oxidation catalytic activity can occur at much lower potential compared to other sensors, which are mostly based on the elemental metal or its oxide. Additionally, the coexistence of Ni and Co in these catalysts can influence the local site oxidation by modulating the electron densities around the active sites.<sup>60</sup> Secondly the chalcogenide coordination also increases the lattice covalency leading to the selenides being more metallic with higher conductivity compared to the oxides. Hence, charge transfer within the catalyst grains is greatly enhanced. The inter-grain charge transfer is also improved significantly by the addition of rGO, which has a synergistic effect, as well as the porous 3D network of the Ni foam leading to high

oxidation current density. The presence of  $\text{Ni}^{3+}$  in the as-synthesized product is also believed to significantly improve the catalytic activity since  $\text{Ni}^{3+}$  is the actual catalytically active site for these electrochemical processes including conversion of glucose to gluconolactone.<sup>61,62</sup> In other Ni-based electrocatalysts, Ni is present mostly as  $\text{Ni}^{2+}$ , which is electrochemically oxidized *in situ* to  $\text{Ni}^{3+}$  (a step commonly known as catalyst activation). The combined effect of these factors results in onset of the catalytic activity at very low applied potentials along with achieving high current density, which is reflected in the sensitivity of the sensor.

### 3.4 Selectivity and stability studies of the $\text{CoNi}_2\text{Se}_4\text{-rGO@NF}$

The two main challenging aspects of non-enzymatic glucose sensing are the effect of possible physiological interference from interferents present in blood serum and the stability of the electrode for long-term use. The relatively high working potential employed to oxidize glucose in conventional sensors can possibly oxidize other compounds present in blood, therefore resulting in an overestimated amperometric current value, which may have life threatening consequences such as hyperglycaemia and hypoglycaemia causing coma or even death. Several compounds found in human blood can interfere with glucose detection as they are strong reducing agents similar to glucose, and hence can easily be oxidized at the selected potential. Such common interfering species include ascorbic acid (AA), lactose (LA), fructose (FR), dopamine (DA), NaCl, KCl and urea. Thus, an experiment was designed to investigate the selectivity of the  $\text{CoNi}_2\text{Se}_4\text{-rGO@NF}$  glucose sensing device towards glucose oxidation and the results are shown in Fig. 5a. The selectivity study was carried out at an applied potential of 0.35 V vs. Ag|AgCl under the same experimental conditions as mentioned above, where glucose and the interferents were added to the same electrolyte. The  $\text{CoNi}_2\text{Se}_4\text{-rGO@NF}$  electrode exhibits a high current response upon the addition of 1.0 mM glucose. However, the addition of 0.1 mM of

the interfering compounds did not yield any detectable current response, as shown in Fig. 5a. This confirmed that the present  $\text{CoNi}_2\text{Se}_4\text{-rGO@NF}$  electrode is selective towards glucose oxidation and can avoid interference from AA, FR, LA, DA, NaCl, KCl and urea. The selectivity of this sensor was also evaluated in the presence of a high concentration of DA and AA by measuring the CV plots in the presence of 1 mM DA, 1 mM AA, or 1 mM glucose solutions at the same potential (0.35 V) as shown in Fig. S7, ESI.† It was observed that at 0.35 V, glucose was oxidized readily producing nearly double the current density compared to that of DA and AA. The CV plots of DA and AA, on the other hand, demonstrated that the onset of electro-oxidation for these compounds was at a much higher potential. This further confirms the high selectivity of  $\text{CoNi}_2\text{Se}_4\text{-rGO@NF}$  towards glucose oxidation at a low applied potential even in the presence of high concentrations of interferents. The peak current density in CV is also an illustration of the sensitivity of the device, and represents the saturation current density that can be achieved in the presence of 1 mM glucose in the solution.

The reproducibility and consistency of the results for  $\text{CoNi}_2\text{Se}_4\text{-rGO@NF}$  towards glucose sensing were investigated by chronoamperometry studies for four different electrodes prepared in three different batches of freshly prepared  $\text{CoNi}_2\text{Se}_4\text{-rGO}$  samples, and one previously tested electrode stored at room temperature for over three months under ambient conditions. The glucose oxidation with these electrodes was measured in 0.1 M NaOH by subsequent addition of 0.01 mM glucose at regular intervals and recording the current responses after each injection. The results are shown in Fig. 5b. It can be observed that addition of a similar concentration of glucose resulted in an almost equal jump in current density and almost the same response time, confirming good repeatability of the  $\text{CoNi}_2\text{Se}_4\text{-rGO@NF}$  electrode. Interestingly, even after three months of storage under ambient conditions, the sensor did not show any significant loss in amperometric response, confirming the excellent reliability of this electrode.

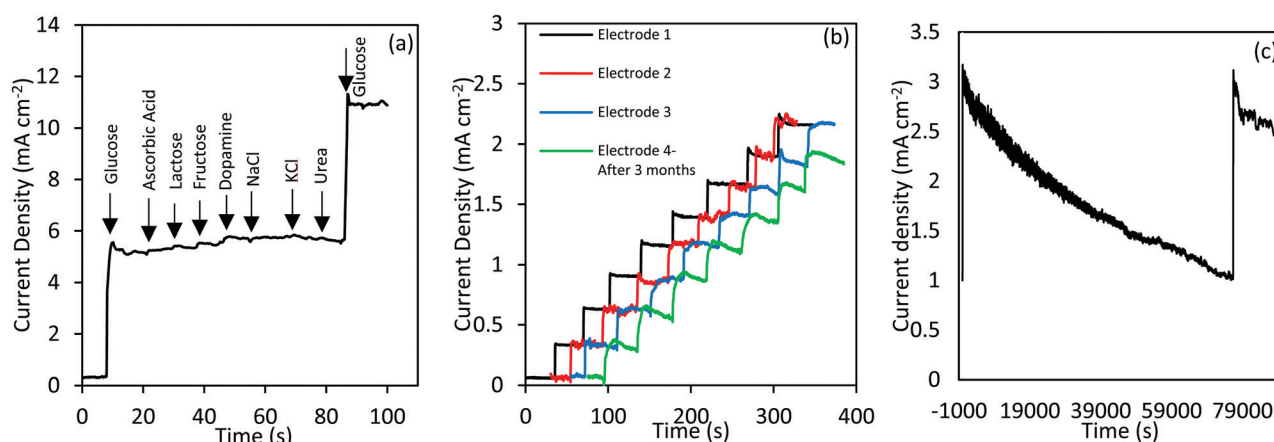


**Fig. 5** (a) The amperometric response of the  $\text{CoNi}_2\text{Se}_4\text{-rGO}$  on NF electrode to the successive addition of 1.0 mM glucose, and 0.1 mM ascorbic acid, lactose, fructose, dopamine, NaCl, KCl and urea. (b) The amperometric response of different batches of freshly prepared electrodes (electrodes 1, 2, and 3, and a previously used electrode stored for 3 months under ambient conditions (electrode 4)) to 0.01 mM successive additions of glucose in 0.1 M NaOH at a working potential of 0.35 V vs. Ag|AgCl. (c) Chronoamperometric long-term stability check at 0.35 V.



The long-term stability of the electrode was also examined by a chronoamperometry test as shown in Fig. 5c, where 0.1 mM glucose was added to 0.1 M NaOH for an extended period of time in an electrolyte containing 1.0 mM glucose. As the glucose in the electrolyte got oxidized, the current density gradually decreased; however, upon addition of fresh glucose into the electrolyte after about 80 000 seconds, it showed an almost identical change in current density to the pristine electrode. This amperometric test underlined the stability of this electrode and verified that there is no surface poisoning and deterioration in efficiency following long-term application. The re-usability and reproducibility of this non-enzymatic glucose sensor are a significant advantage over enzymatic sensors, which have limited reusability due to enzyme denaturation.

A comparison of the CoNi<sub>2</sub>Se<sub>4</sub>-rGO@NF glucose sensing efficiency with that of several previously reported enzymatic and non-enzymatic glucose biosensors is provided in Table 1. From this table it can be concluded that CoNi<sub>2</sub>Se<sub>4</sub>-rGO@NF indeed shows promising glucose sensing activities at a low operating voltage, with a low limit of detection, high sensitivity and fast response time along with a wide linear range. These characteristics collectively are indicative of an excellent performance of CoNi<sub>2</sub>Se<sub>4</sub>-rGO@NF as a non-enzymatic glucose sensor.

#### 4. Application of the CoNi<sub>2</sub>Se<sub>4</sub>-rGO@NF electrode towards detection of human blood glucose

The practical application of the CoNi<sub>2</sub>Se<sub>4</sub>-rGO@NF sensor was verified by detecting the glucose concentration in a few drops of blood obtained from participating volunteers and the results were compared with those measured using a store-bought glucometer kit (ReliOn<sup>®</sup> containing typical glucose sensing strips and the meter). Details of this measurement along with the relevant plots are provided in the ESI.<sup>†</sup> Specifically, 100  $\mu$ L of 1 mM glucose solution was added two times to 0.05 M NaOH to stabilize the CoNi<sub>2</sub>Se<sub>4</sub>-rGO@NF electrode response. Then, the blood sample was directly injected into the electrolytic system followed by two more additions of equal volumes of 1 mM glucose. The current response for each of these additions (1 mM glucose solution) was plotted as a function of glucose concentration and the glucose amount in the blood sample was estimated from the linear fit of the plot (after subtracting the background glucose concentrations). A typical plot for the blood glucose experiment is shown in Fig. S8, ESI,<sup>†</sup> while Table 2 lists the glucose concentration as detected by a standard glucometer and the CoNi<sub>2</sub>Se<sub>4</sub>-rGO-based sensor. As can be seen from

the table, the estimated concentration using the sensor was in good agreement with the value measured by the commercial glucometer (ReliOn), indicating that the CoNi<sub>2</sub>Se<sub>4</sub>-rGO@NF electrode can be utilized for practical glucose detection in blood samples. Three measurements were performed for each sample and an acceptable relative standard deviation (RSD) of less than 5% was achieved for both samples, suggesting the reliability of this electrode for glucose sensing.

## 5. Conclusions

We have demonstrated a simple approach for producing CoNi<sub>2</sub>Se<sub>4</sub>-rGO on Ni Foam by a facile electrodeposition method producing a catalyst-coated and binder-free composite electrode. The as-deposited CoNi<sub>2</sub>Se<sub>4</sub> exhibited a nanoflake-like geometry with a uniform and highly 3-dimensional network of the catalytic film. Moreover, the multiple active sites in CoNi<sub>2</sub>Se<sub>4</sub> combined with the enhanced conductivity of the reduced graphene oxide improved the electrocatalytic performance of this electrode towards glucose oxidation. The ultrahigh sensitivity (18.89 mA mM<sup>-1</sup> cm<sup>-2</sup>) at a low applied potential of only 0.35 V vs. Ag|AgCl, wide linear range (1  $\mu$ M–4.0 mM), low detection limit (0.65  $\mu$ M), short response time of less than 4 seconds with impressive selectivity, repeatability, and stability make this CoNi<sub>2</sub>Se<sub>4</sub>/rGO-NF a promising electrode to serve as a non-enzymatic glucose sensor. Moreover, the reliability of this electrochemical glucose sensor was tested by estimating the blood glucose level in two independent blood samples, and the values showed excellent similarity with the glucose level detected by a commercially available glucometer, indicating that these biosensors indeed have great potential for practical use.

## Conflicts of interest

There are no conflicts to declare.

## Acknowledgements

This work was partially supported through funds from the National Science Foundation (DMR 1710313). The authors would like to thank Dr Sergii Chertopalov for help with Raman spectroscopy.

## Notes and references

- 1 H. Rao, Z. Zhang, H. Ge, X. Liu, P. Zou, X. Wang and Y. Wang, *New J. Chem.*, 2017, **41**, 3667–3676.
- 2 K.-L. Wu, Y.-M. Cai, B.-B. Jiang, W.-C. Cheong, X.-W. Wei, W. Wang and N. Yu, *RSC Adv.*, 2017, **7**, 21128–21135.
- 3 N. Hui and J. Wang, *J. Electroanal. Chem.*, 2017, **798**, 9–16.
- 4 B. Xue, K. Li, L. Feng, J. Lu and L. Zhang, *Electrochim. Acta*, 2017, **239**, 36–44.
- 5 S. Ci, T. Huang, Z. Wen, S. Cui, S. Mao, D. A. Steeber and J. Chen, *Biosens. Bioelectron.*, 2014, **54**, 251.
- 6 A. Sun, J. Zheng and Q. Sheng, *Electrochim. Acta*, 2012, **65**, 64.
- 7 A. Heller and B. Feldman, *Chem. Rev.*, 2008, **108**, 2482–2505.

Table 2 Determination of glucose in human blood

Sample	Measured concentration (mM)		Deviation (%)
	Commercial glucometer	The developed electrode (RSD%)	
1	5.66 (102 mg dL <sup>-1</sup> )	5.56 (4.12%)	1.76
2	5.38 (97 mg dL <sup>-1</sup> )	5.27 (4.36%)	2.04

- 8 H. Susanto, A. M. Samsudin, N. Rokhati and I. N. Widiassa, *Enzyme Microb. Technol.*, 2013, **52**, 386–392.
- 9 K. Kumar Naik, A. Gangan, B. Chakraborty, S. K. Nayak and C. S. Rout, *ACS Appl. Mater. Interfaces*, 2017, **9**, 23894–23903.
- 10 G. Dryhurst and K. Niki, *Redox Chemistry and Interfacial Behavior of Biological Molecules*, Springer, USA, 2012.
- 11 F. P. Van der Zee and F. J. Cervantes, *Biotechnol. Adv.*, 2009, **27**, 256–277.
- 12 X. Chia, A. Y. S. Eng, A. Ambrosi, S. M. Tan and M. Pumera, *Chem. Rev.*, 2015, **115**, 11941–11966.
- 13 J. L. Qi, X. Wang, J. H. Lin, F. Zhang, J. C. Feng and W. D. Fei, *J. Mater. Chem. A*, 2015, **3**, 12396–12403.
- 14 W. Huang, Y. Cao, Y. Chena, J. Peng, X. Lai and J. Tu, *Appl. Surf. Sci.*, 2017, **396**, 804–811.
- 15 V. Neburchilov, H. Wang, J. J. Martin and Q. Wei, *J. Power Sources*, 2010, **195**, 1271–1291.
- 16 P. Karthick Kannan and C. S. Rout, *Chem. – Eur. J.*, 2015, **21**, 9355–9359.
- 17 B. G. Amin, A. T. Swesi, J. Masud and M. Nath, *Chem. Commun.*, 2017, **53**, 5412–5415.
- 18 A. Sivanantham, P. Ganesan and S. Shanmugam, *Adv. Funct. Mater.*, 2016, **26**, 4661–4672.
- 19 D. Liu, Q. Lu, Y. Luo, X. Sun and A. M. Asiri, *Nanoscale*, 2015, **7**, 15122–15126.
- 20 Q. Liu, J. Jin and J. Zhang, *ACS Appl. Mater. Interfaces*, 2013, **5**, 5002–5008.
- 21 S. Yun Khoo, J. Miao, H. Yang, Z. B. He, K. C. Leong, B. Liu and T. T. Yang Tan, *Adv. Mater. Interfaces*, 2015, **2**, 1500384.
- 22 N. Huang, S. Zhang, H. Huang, J. Liu, Y. Sun, P. Sun, C. Bao, L. Zheng, X. Sun and X. Zhao, *Electrochim. Acta*, 2016, **192**, 521–528.
- 23 J. Lin and S. Chou, *Electrochem. Commun.*, 2013, **37**, 11–14.
- 24 R. Zou, Z. Zhang, M. Fung Yuen, M. Sun, J. Hu, C. Lee and W. Zhang, *NPG Asia Mater.*, 2015, **7**, 8.
- 25 Q. Wang, L. Jiao, Y. Han, H. Du, W. Peng, Q. Huan, D. Song, Y. Si, Y. Wang and H. Yuan, *J. Phys. Chem. C*, 2011, **115**, 8300–8304.
- 26 L. Shen, J. Wang, G. Xu, H. Li, H. Dou and X. Zhang, *Adv. Energy Mater.*, 2015, **5**, 1400977.
- 27 J. Pu, T. Wang, H. Wang, Y. Tong, C. Lu, W. Kong and Z. Wang, *ChemPlusChem*, 2014, **79**, 577–583.
- 28 J. Xiao, L. Wan, S. Yang, F. Xiao and S. Wang, *Nano Lett.*, 2014, **14**, 831–838.
- 29 H. Wan, J. Jiang, J. Yu, K. Xu, L. Miao, L. Zhang, H. Chen and Y. Ruan, *CrystEngComm*, 2013, **15**, 7649–7651.
- 30 S. Peng, L. Li, C. Li, H. Ta, R. Caia, H. Yu, S. Mhaisalkar, M. Srinivasan, S. Ramakrishna and Q. Yan, *Chem. Commun.*, 2013, **49**, 10178–10180.
- 31 A. T. Swesi, J. Masud, W. P. R. Liyanage, S. Umapathi, E. Bohannan, J. Medvedeva and M. Nath, *Sci. Rep.*, 2017, **7**, 2401.
- 32 P. K. Kannan, B. Dinesh, C. Y. An and C.-H. Chung, *ChemistrySelect*, 2017, **2**, 1967–1973.
- 33 L. Zhang, Y. Ding, R. Li, C. Ye, G. Zhao and Y. Wang, *J. Mater. Chem. B*, 2017, **5**, 5549–5555.
- 34 G. F. Wang, X. P. He, L. L. Wang, A. X. Gu, Y. Huang, B. Fang, B. Y. Geng and X. J. Zhang, *Microchim. Acta*, 2013, **180**, 161–186.
- 35 K. E. Toghill and R. G. Compton, *Int. J. Electrochem. Sci.*, 2010, **5**, 1246–1301.
- 36 P. K. Kannan and C. S. Rout, *Chem. – Eur. J.*, 2015, **21**, 9355–9359.
- 37 K. E. Toghill and R. G. Compton, *Int. J. Electrochem. Sci.*, 2010, **5**, 1246–1301.
- 38 J. L. Gautier, E. Rios, M. Gracia, J. F. Marco and J. R. Gancedo, *Thin Solid Films*, 1997, **311**, 51–57.
- 39 Y. Chen, Y. Li, D. Sun, D. Tian, J. Zhang and J. J. Zhu, *J. Mater. Chem.*, 2011, **21**, 7604.
- 40 J. J. Gooding, *Electrochim. Acta*, 2005, **50**, 3049.
- 41 L. Wu, L. Feng, J. Ren and X. Qu, *Biosens. Bioelectron.*, 2012, **34**, 57.
- 42 D. Chen, L. Tang and J. Li, *Chem. Soc. Rev.*, 2010, **39**, 3157.
- 43 D. Chen, H. Feng and J. Li, *Chem. Rev.*, 2012, **112**, 6027.
- 44 S. Bong, Y. R. Kim, I. Kim, S. Woo, S. Uhm, J. Lee and H. Kim, *Electrochem. Commun.*, 2010, **12**, 129.
- 45 D. C. Marcano, D. V. Kosynkin, J. M. Berlin, A. Sinitskii, Z. Sun, A. Slesarev, L. B. Alemany, W. Lu and J. M. Tour, *ACS Nano*, 2010, **4**(8), 4806–4814.
- 46 G. Li, H. Huo and C. Xu, *J. Mater. Chem. A*, 2015, **3**, 4922.
- 47 J. Liu, W. Lv, W. Wei, C. Zhang, Z. Li, B. Li, F. Kang and Q.-H. Yang, *J. Mater. Chem. A*, 2014, **2**, 3031–3037.
- 48 B. Zhan, C. Liu, H. Chen, H. Shi, L. Wang, P. Chen, W. Huang and X. Dong, *Nanoscale*, 2014, **6**, 7424–7429.
- 49 M. Gao, Y. Xu, J. Jiang, Y. Zheng and S. Yu, *J. Am. Chem. Soc.*, 2012, **134**, 2930.
- 50 C. Jin, F. Lu, X. Cao, Z. Yang and R. Yang, *J. Mater. Chem. A*, 2013, **1**, 12170.
- 51 T. Z. Su, Q. Z. Xu, G. F. Chen, H. Cheng, N. Li and Z. Q. Liu, *Electrochim. Acta*, 2015, **174**, 1216.
- 52 H. Shi and G. Zhao, *J. Phys. Chem. C*, 2014, **118**, 25939.
- 53 E. Umeshbabu, G. Rajeshkhanna, P. Justin and G. Ranga Rao, *RSC Adv.*, 2015, **5**, 66657.
- 54 A. B. Mandale, S. Badrinarayanan, S. K. Date and A. P. B. Sinha, *J. Electron Spectrosc. Relat. Phenom.*, 1984, **33**, 61.
- 55 X.-C. Dong, H. Xu, X.-W. Wang, Y.-X. Huang, M.-B. Chan-Park, H. Zhang, L.-H. Wang, W. Huang and P. Chen, *ACS Nano*, 2012, **6**, 3206–3213.
- 56 L. Zhang, Y. Ding, R. Li, C. Ye, G. Zhao and Y. Wang, *J. Mater. Chem. B*, 2017, **5**, 5549.
- 57 K. Tian, M. Prestgard and A. Tiwari, *Mater. Sci. Eng. Carbon*, 2014, **41**, 100–118.
- 58 U. De Silva, J. Masud, N. Zhang, Y. Hong, W. P. R. Liyanage, M. Asle Zaeem and M. Nath, *J. Mater. Chem. A*, 2018, **6**, 7608–7622.
- 59 S. Umapathi, J. Masud, A. T. Swesi and M. Nath, *Adv. Sustainable Syst.*, 2017, **1**, 1700086.
- 60 X. Cao, Y. Hong, N. Zhang, Q. Chen, J. Masud, M. Asle Zaeem and M. Nath, *ACS Catal.*, 2018, **8**(9), 8273–8289.
- 61 C. Chen, M. Shi, M. Xue and Y. Hu, *RSC Adv.*, 2017, **7**, 22208–22214.
- 62 F. J. Garcia-Garcia, P. Salazar, F. Yubero and A. R. González-Elipe, *Electrochim. Acta*, 2016, **201**, 38–44.

- 63 X.-Y. Lang, H.-Y. Fu, C. Hou, G.-F. Han, P. Yang, Y.-B. Liu and Q. Jiang, *Nat. Commun.*, 2013, **4**, 2169.
- 64 Z. Zhuang, X. Su, H. Yuan, Q. Sun, D. Xiao and M. M. F. Choi, *Analyst*, 2008, **133**, 126–132.
- 65 X. Zhu, Q. Jiao, C. Zhang, X. Zuo, X. Xiao, Y. Liang and J. Nan, *Microchim. Acta*, 2013, **180**, 477–483.
- 66 M. R. Mahmoudian, W. J. Basirun, P. M. Woi, M. Sookhakian, R. Yousefi, H. Ghadimi and Y. Alias, *Mater. Sci. Eng. Carbon*, 2016, **59**, 500–508.
- 67 K. K. Naik, S. Kumar and C. S. Rout, *RSC Adv.*, 2015, **5**, 74585–74591.
- 68 X. Liua, W. Yanga, L. Chena and J. Jiaa, *Electrochim. Acta*, 2017, **235**, 519–526.
- 69 Z. Cui, H. Yin and Q. Nie, *J. Alloys Compd.*, 2015, **632**, 402–407.
- 70 W. Zhu, J. Wang, W. Zhang, N. Hu, J. Wang, L. Huang, R. Wang, Y. Suo and J. Wang, *J. Mater. Chem. B*, 2018, **6**, 718–724.
- 71 H. Xu, C. Xia, S. Wang, F. Han, M. K. Akbari, Z. Hai and S. Zhuiykov, *Sens. Actuators, B*, 2018, **267**, 93–103.
- 72 X. Wang, H. Jian, Q. Xiao and S. Huang, *Appl. Surf. Sci.*, 2018, **459**, 40–47.
- 73 X. Niu, M. Lan, H. Zhao and C. Chen, *Anal. Chem.*, 2013, **85**, 3561–3569.
- 74 M. Wu, S. Meng, Q. Wang, W. Si, W. Huang and X. Dong, *ACS Appl. Mater. Interfaces*, 2015, **7**, 21089–21094.
- 75 L. Wang, X. Lu, Y. Ye, L. Sun and Y. Song, *Electrochim. Acta*, 2013, **114**, 484–493.
- 76 G. Li, H. Huo and C. Xu, *J. Mater. Chem. A*, 2015, **3**, 4922–4930.
- 77 F. Huang, Y. Zhong, J. Chen, S. Li, Y. Li, F. Wang and S. Feng, *Anal. Methods*, 2013, **5**, 3050–3055.
- 78 X. Tang, B. Zhang, C. Xiao, H. Zhou, X. Wang and D. He, *Sens. Actuators, B*, 2016, **222**, 232–239.
- 79 G. Zeng, W. Li, S. Ci, J. Jia and Z. Wen, *Sci. Rep.*, 2016, **6**, 36454.
- 80 H. Liu, X. Wu, B. Yang, Z. Li, L. Lei and X. Zhang, *Electrochim. Acta*, 2015, **174**, 745–752.
- 81 N. Hui, S. Wang, H. Xie, S. Xu, S. Niu and X. Luo, *Sens. Actuators, B*, 2015, **221**, 606–613.
- 82 S. Mani, S. Ramaraj, S.-M. Chen, B. Dinesh and T.-W. Chen, *J. Colloid Interface Sci.*, 2017, **507**, 378–385.
- 83 P. K. Kannan, C. Hu, H. Morgan and C. S. Rout, *Chem. – Asian J.*, 2016, **11**, 1837–1841.
- 84 M. A. Kiani, M. AbbasniaTehrani and H. Sayahi, *Anal. Chim. Acta*, 2014, **839**, 26–33.
- 85 C. Xu, Y. Cao, Y. Chen, W. Huang, D. Chen, Q. Huang and J. Tu, *Eur. J. Inorg. Chem.*, 2016, 3163–3168.
- 86 L. Zhang, C. Ye, X. Li, Y. Ding, H. Liang, G. Zhao and Y. Wang, *Nano-Micro Lett.*, 2018, **10**, 28.
- 87 T.-W. Lin, C.-J. Liu and C.-S. Dai, *Appl. Catal., B*, 2014, **154–155**, 213–220.
- 88 S. Kim, S. H. Lee, M. Cho and Y. Lee, *Biosens. Bioelectron.*, 2016, **85**, 587–595.
- 89 H. Huo, Y. Zhaoa and C. XuSdfsd, *J. Mater. Chem. A*, 2014, **2**, 15111–15117.
- 90 X. Luo, M. Huang, L. Bie, D. He, Y. Zhangb and P. Jiang, *RSC Adv.*, 2017, **7**, 23093–23101.
- 91 B. Wang, Y. Cao, Y. Chen, X. Lai, J. Peng, J. Tu and X. Li, *Nanotechnology*, 2017, **28**, 025501.
- 92 E. Zhang, Y. Xie, S. Ci, J. Jia and Z. Wen, *Biosens. Bioelectron.*, 2016, **81**, 46–53.
- 93 Y. Zhang, L. Luo, Z. Zhang, Y. Ding, S. Liu, D. Deng, H. Zhao and Y. Chen, *J. Mater. Chem. B*, 2014, **2**, 529–535.
- 94 B. Xue, K. Li, L. Feng, J. Lu and L. Zhang, *Electrochim. Acta*, 2017, **239**, 36–44.
- 95 Y. Ding, Y. Wang, L. Su, M. Bellagamba, H. Zhang and Y. Lei, *Biosens. Bioelectron.*, 2010, **26**, 542–548.
- 96 C. Lee, S. H. Lee, M. Cho and Y. Lee, *Microchim. Acta*, 2016, **183**, 3285–3292.
- 97 R. Boukherroub and S. Szunerits, *J. Mater. Chem. A*, 2014, **2**, 5525–5533.
- 98 Y. Liu, X. Cao, R. Kong, G. Du, A. M. Asiri, Q. Lu and X. Sun, *J. Mater. Chem. B*, 2017, **5**, 1901–1904.
- 99 K. Ghanbari and Z. Babaei, *Anal. Biochem.*, 2016, **498**, 37–46.
- 100 Y. Zhang, Y. Wang, J. Jia and J. Wang, *Sens. Actuators, B*, 2012, **171**, 580–587.
- 101 A. Sun, J. Zheng and Q. Sheng, *Sens. Actuators, B*, 2012, **65**, 64–69.
- 102 H. Yang and Y. Zhu, *Biosens. Bioelectron.*, 2007, **22**, 2989–2993.
- 103 R. Kumar, T. Bhuvana, P. Rai and A. Sharma, *J. Electrochem. Soc.*, 2018, **165**(2), B1–B8.
- 104 R. Ahmad, N. Tripathy, M.-S. Ahn, K. S. Bhat, T. Mahmoudi, Y. Wang, J.-Y. Yoo, D.-W. Kwon, H.-Y. Yang and Y.-B. Hahn, *Sci. Rep.*, 2017, **7**, 5715.
- 105 C. Zhao, X. Wu, X. Zhang, P. Li and X. Qian, *J. Electroanal. Chem.*, 2017, **785**, 172–179.
- 106 X. Lia, J. Liu, X. Ji, J. Jiang, R. Ding, Y. Hu, A. Hu and X. Huang, *Sens. Actuators, B*, 2010, **147**, 241–247.
- 107 Z. D. Gao, J. Guo, N. K. Shrestha, R. Hahn, Y. Y. Song and P. Schmuki, *Chem. – Eur. J.*, 2013, **19**, 15530–15534.